Substrate-Controlled Photothermal Properties of Femtosecond Laser-Fabricated Zirconium Nitride Periodic Structures

Xuran Wang(汪煦然)[1] , Jingya Sun(孙靖雅)[1,2,†], Binhang Gao(高彬航)[1], and Yang Yang(杨洋)[3]

[1] *Laser Micro/Nano Fabrication Laboratory, School of Mechanical Engineering, Beijing Institute of Technology, Beijing 100081 China*
[2]*Yangtze Delta Region Academy of Beijing Institute of Technology, Jiaxing 314000, China*
[3]*Beijing National Laboratory for Condensed Matter Physics, Institute of Physics, Chinese Academy of Sciences, P.O. Box 603, Beijing 100190, China; yang.yang@iphy.ac.cn*

Zirconium nitride (ZrN), a typical refractory transition metal nitride, is characterized by excellent plasmonic properties, high-temperature stability and mechanical properties. It has been demonstrated to have tremendous application potential in fields such as photothermal conversion and solar energy utilization. However, limitations including poor structural consistency and low processing efficiency are encountered in its application. Moreover, the synergistic regulation mechanism of micro-nano structures and substrate materials toward photothermal performance remains unclear. A method for preparing high-performance ZrN photothermal thin films through femtosecond laser substrate regulation is proposed in this paper, and the fabrication of ZrN thin films with laser-induced periodic surface structures (LIPSS) is achieved with high efficiency and high uniformity. The regulation laws of the aspect ratio of LIPSS and the parallel and perpendicular polarizations of light sources on photothermal conversion capability are systematically investigated using the finite-difference time-domain (FDTD) method, and it is revealed that a high aspect ratio can significantly enhance the photothermal capability under all polarization conditions. Comparative photothermal experiments are carried out on ZrN thin films on silicon (Si) and titanium (Ti) substrates with LIPSS, and the enhancement effect of a high aspect ratio on photothermal capability was verified. Excellent linear relationships between temperature rise magnitude and light intensity are observed for ZrN thin films on Si and Ti substrates with LIPSS, with correlation coefficients of 0.996 and 0.984, respectively. Meanwhile, outstanding photothermal stability is demonstrated for both samples during multiple thermal cycles within 600 s, and ZrN thin films on Si substrates with LIPSS can be rapidly heated to 50 °C within 60 s under 2.5 Sun irradiation. Furthermore, the analysis of heat transfer mechanisms in different substrates verifies that materials with high thermal conductivity can better exert the photothermal capability of ZrN thin films. The photothermal conversion mechanism of periodic ZrN structures and the regulation law of substrate thermal conductivity on temperature field distribution are revealed in this work. The intrinsic mechanism of improving ZrN photothermal performances through femtosecond laser substrate regulation is clarified, and a theoretical basis is provided for the structural design and material selection of ZrN photothermal devices.

† Corresponding author. E-mail: sjy@bit.edu.cn

Keywords: Femtosecond Laser, Photothermal Conversion, Substrate Regulation, Zirconium Nitride Thin Films, LIPSS, FDTD Simulation

1. Introduction

ZrN, as a typical refractory transition metal nitride, is endowed with excellent plasmonic properties, high-temperature stability and mechanical properties[1-4]. It is regarded as an ideal substitute for noble metal plasmonic materials[5–7]. Tremendous application potential has been demonstrated in fields such as photothermal conversion and solar energy utilization[8–14]. Despite its numerous outstanding properties, significant challenges are encountered by traditional processing schemes in the fabrication of micro/nanostructures for application-oriented manufacturing. Fabrication of complex and delicate structures is challenging. Stress concentration or thermal stress accumulation is often present after processing. To address these difficulties, femtosecond laser is adopted as an ultrafast precision processing tool. Unique advantages have been exhibited in micro/nanofabrication of various materials, performance modulation and minimal heat-affected zone generation[15–17]. It has been recognized as an effective approach for processing high-hardness materials[18–24].

Recent advances have further extended femtosecond laser processing beyond conventional direct writing and surface ablation. Spatiotemporal optical-field modulation, including Bessel-beam shaping and burst-pulse modulation, has enabled high-throughput fabrication of large-area microstructure arrays with improved aspect-ratio control, processing consistency, and tolerance to focal-position variations[25]. The integration of machine learning with femtosecond laser processing has also established predictive relationships among processing parameters, structural morphology, and optical performance, thereby enabling rapid customization of functional optical surfaces[26]. In addition, burst-mode temporal shaping has been applied to regulate energy deposition and interfacial dynamics during the joining of rough transparent–metal heterogeneous materials[27]. These developments demonstrate that femtosecond lasers can provide not only precise material removal but also programmable control over structural geometry, optical functionality, and heterogeneous interfaces.

In this context, substrate-first femtosecond laser regulation offers a complementary route for transferring laser-induced surface morphology to a subsequently deposited functional film. Here, we employ this strategy to regulate the morphology and photothermal response of ZrN coatings deposited on LIPSS-patterned Si and Ti substrates.

Material ablation can be achieved by femtosecond laser within an extremely short time duration. Therefore, complex nanoscale structures can be fabricated. Meanwhile, it has been widely employed for the processing of microstructures in thin film materials[28–31]. However, the influences of fabricated nanoscale structures such as the period of LIPSS, the structural dimensions and the aspect ratio in a single period on photothermal conversion remain unclear. For thin film materials, the effects of substrate morphology, thermal conductivity and the heat transfer mode between the film and the substrate on the photothermal application are required to be further

investigated. In addition, research gaps still remain in the synergistic regulation of LIPSS and thin film substrates. Detailed mechanisms underlying the photothermal applications of ZrN thin films are in urgent need of in-depth investigation, aiming to further improve the solar energy utilization efficiency of ZrN.

A fabrication method for ZrN thin films based on femtosecond laser substrate modulation is proposed in this paper. By means of the synergistic regulation of LIPSS and substrate thermal conductivity on photothermal conversion, high-performance ZrN photothermal thin films are successfully fabricated. LIPSS are induced on the substrate materials by femtosecond laser. When combined with the magnetron sputtering coating technique, large-area and uniform ZrN thin films are obtained. The photothermal measurements show that the ZrN-coated samples prepared on LIPSS-patterned substrates exhibit greater temperature rises than their coated smooth-substrate counterparts under the tested irradiation conditions. The aspect ratio of the LIPSS structures exerts a significant influence on the photothermal performance. Meanwhile, distinct heat transfer mechanisms of the two substrates are revealed. Enhanced photothermal conversion efficiency is achieved for ZrN thin films on Si substrates with LIPSS of higher aspect ratio. For the ZrN thin films on the high-thermal-conductivity Si substrate, heat can be rapidly transferred from the ZrN thin films to the substrate, and thus the maximum temperature occurs on the light-receiving top surface of the thin film. For the ZrN thin films on the low-thermal-conductivity Ti substrate, heat is accumulated at the interface between the thin film and the substrate. This results in the maximum temperature being located at the interface. These findings facilitate the in-depth understanding of the heat transfer mechanism of ZrN in photothermal conversion. A theoretical foundation is provided for the development of ZrN photothermal conversion devices.

2. EXPERIMENTAL SECTION

Uniform LIPSS are fabricated on 10×10 mm smooth Si and Ti wafers using a femtosecond laser with a wavelength of 1030 nm and a pulse duration of 264 fs in this study. Because LIPSS formation depends on the optical, thermal, and mechanical response of the irradiated material, the processing windows were optimized independently to obtain stable and spatially uniform LIPSS on each substrate. The processing parameters for Si wafers were therefore set to a laser fluence of 0.86 J cm^{-2} and a scanning speed of 1000 μm s^{-1}, whereas those for Ti wafers were set to 2.84 J cm^{-2} and 1600 μm s^{-1}, respectively. These parameter sets should not be interpreted as chemically equivalent laser treatments. Subsequently, 200-nm-thick ZrN films were deposited on the LIPSS-structured and smooth Si and Ti substrates using the same nominal magnetron-sputtering conditions described below. The specific deposition process parameters are as follows. CK300-type gas coating equipment was adopted. And a ZrN target with a diameter of 2 inches was used as the sputtering source, which was fixed at the cathode position of the magnetron sputtering system. Si wafers and Ti wafers were selected as the substrates, and the uniformity of thin film deposition was ensured by the rotation of the rotating holder. The deposition process was carried out at room temperature, with a fixed target-to-substrate distance

of 80 mm. Argon gas with a purity of 99% was used as the deposition gas. Before deposition, the chamber base pressure was pumped down to 1×10^{-4}Pa, and the influence of residual gas in the chamber on the thin film quality was reduced through multiple cyclic pumping operations. Finally, ZrN thin films were successfully fabricated under the conditions of a working pressure of 1.5 Pa and a power density of 9.1 W/cm² with continuous deposition for 1200 s.

The surface morphologies of the LIPSS-structured samples before and after ZrN thin film deposition are shown in Fig. 1 It can be observed that the as-fabricated LIPSS remain clearly visible after ZrN thin film deposition via magnetron sputtering. This indicates that ZrN is uniformly deposited on the protrusions and depressions within the LIPSS periods during the deposition process. The morphology of the ZrN thin films is thus consistent with that of the underlying substrates. Quantitative LIPSS morphology was obtained from the calibrated height channels of the confocal laser scanning microscopy data. Five independent fields were analysed for the laser-processed Ti substrates, and four independent fields were analysed for the laser-processed Si substrates. Each 1024 × 1024 height map covered approximately 128 × 128 μm and was divided into 16 non-overlapping subregions. After least-squares plane levelling, the long-wavelength scan-track background was removed to isolate the fine LIPSS component. The period, Λ, was determined from the dominant two-dimensional spatial-frequency peak. The robust peak-to-valley height, H, was calculated from the 95th-to-5th-percentile range of the oriented LIPSS height component. The effective lateral length, L, and width, W, were defined as the 1/e autocorrelation lengths parallel and perpendicular to the LIPSS ridges, respectively. The effective lateral aspect ratio was calculated as L/W, whereas H/Λ was reported separately as the cross-sectional relief ratio. Values for each substrate are reported as the mean ± sample standard deviation across independent fields. Here, L and W denote the effective feature dimensions parallel and perpendicular to the LIPSS ridges, respectively; H is the peak-to-valley height, and Λ is the LIPSS period.

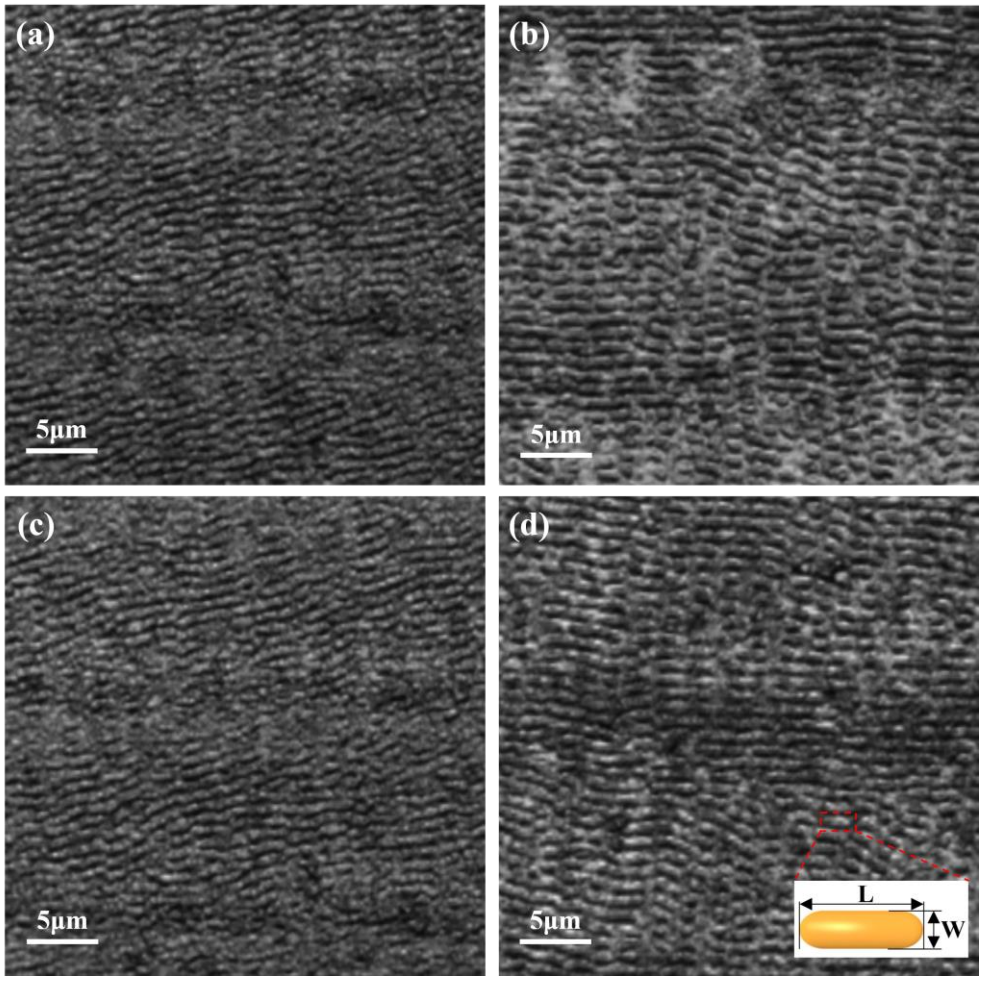


Fig. 1 Confocal laser scanning microscopy images of (a) Si substrates with LIPSS; (b) Ti substrate with LIPSS; (c) ZrN thin films on Si substrates with LIPSS; (d) ZrN thin films on Ti substrates with LIPSS

Differences are observed in the corresponding LIPSS structures due to the distinct material properties of the substrates. Quantitative analysis of the confocal height maps shows that the period Λ, feature width W, peak-to-valley height H, and in-plane aspect ratio L/W were 0.907 ± 0.034 μm, 0.338 ± 0.012 μm, 0.118 ± 0.018 μm, and 12.59 ± 2.01 for Si, respectively, compared with 0.856 ± 0.010 μm, 0.320 ± 0.005 μm, 0.061 ± 0.019 μm, and 8.47 ± 0.60 for Ti. Thus, the two substrates exhibit similar periods and widths, whereas the Si-derived LIPSS have a greater height modulation and a larger L/W. The complete statistics and representative height profiles are provided in Table S1 and Fig. S5. To establish a computationally tractable model, a local elongated feature within one LIPSS period was represented by a capsule-shaped structure consisting of a cylindrical body and two hemispherical end caps, as illustrated in the inset of Fig. 1(d). Here, L and W denote the total length and width of the equivalent capsule, respectively, and L/W defines its aspect ratio. This isolated capsule captures the first-order length and width characteristics of an individual nanorod-like feature but does not reproduce the geometrical continuity or electromagnetic coupling of the periodic LIPSS. It is therefore used only to examine the intrinsic aspect-ratio-dependent response of an individual feature. The influence of periodic coupling and structural continuity is evaluated separately using three-dimensional

periodic-capsule and two-dimensional continuous-ridge models in Section 3.2. As can be seen from Fig. 1**,** a higher aspect ratio is observed for the ZrN thin films on Si substrates with LIPSS, and a lower aspect ratio with variations within a certain range is observed for the ZrN thin films on Ti substrates with LIPSS. It is clear that significant differences are present in the aspect ratios of LIPSS formed on Si and Ti substrates. Furthermore, the thermal conductivity of Si is approximately 150 W/m·K, while that of Ti is about 15 W/m·K. On this basis, Si and Ti are adopted as substrates to clearly demonstrate the effects of the LIPSS aspect ratio, the thermal conductivity of substrate materials, and their synergistic regulation on photothermal conversion capability.

3. RESULTS AND DISCUSSION

3.1. Photothermal Conversion Model

The physical basis of photothermal energy conversion is constituted by the interaction between light and matter at the nanoscale. Spherical nanoparticles are regarded as the classic system for theoretical modeling of photothermal effects due to their geometric symmetry and analytical solvability. A nanosphere with a dielectric constant of ε and a radius of r is considered. It is immersed in a medium with a refractive index of n_s and a dielectric constant of ε_s. It is irradiated by a plane wave with a wavelength of λ. According to classical electrodynamics, the incident light can be regarded as a uniform electric field E_0 at the particle scale. When the quasi-static approximation is satisfied for the sphere, the internal electric field E_{in} of the spherical nanoparticle is given by:

$$E_{\text{in}} = -(\xi - 1) E_0 \tag{1}$$

$$\xi = \frac{\varepsilon - \varepsilon_s}{\varepsilon + 2\varepsilon_s} \tag{2}$$

Where ξ is defined as the enhancement factor, which plays a pivotal role in the fundamental physics of nanoplasmonics.

The intensity ratio between the internal electric field of the particle and the incident electric field can be obtained as follows:

$$\left|\frac{E_{in}}{E_0}\right|^2 = |\xi - 1|^2 = 9\left|\frac{\varepsilon_s}{\varepsilon + 2\varepsilon_s}\right|^2 \tag{3}$$

The core of photothermal conversion is the conversion of incident photon energy into thermal energy by materials. The rate of this energy conversion is characterized by thermal power. The thermal power of nanoparticles q is directly correlated with their optical absorption cross-section σ_{abs} and the incident light intensity I [32]. It is governed by the following equation:

$$q = \sigma_{\text{abs}} I \tag{4}$$

$$I = \frac{1}{2} n_{\text{s}} c_0 \varepsilon |E_0|^2 \tag{5}$$

Where σ_{abs} is defined as the optical absorption cross-section of the nanoparticles. The capability of the material to capture photons and convert them into thermal energy is characterized by this parameter. c_0 is the speed of light, and a value of 3×10^8 m/s is adopted for this physical constant.

Analyzed from the perspective of electromagnetic loss mechanism, the thermal power is proportional to the imaginary part of the material dielectric constant ε'' and the square of the internal electric field intensity. This relationship is given by: $q \propto \varepsilon'' \cdot |E_{in}^2|$.Based on this principle, a dimensionless number Jo was proposed by Lalisse. This parameter is adopted to evaluate the photothermal capability of nanoparticles composed of different materials [33].

$$Jo = \frac{e \cdot \varepsilon''}{n_s} \left| \frac{E_{in}}{E_0} \right|^2 \tag{6}$$

Where e is defined as the photon energy. It satisfies the equation $e = \lambda_{ref}/\lambda$. λ_{ref} is defined as the reference wavelength, a value of approximately 1240 nm is adopted for this physical parameter.

Furthermore, Equation 6 can be extended to nanostructures of arbitrary morphology with a volume of V. This is because the relationship between thermal power and absorption cross-section is given by:

$$qV = \sigma_{abs} \cdot I \tag{7}$$

The dimensionless number Jo can be further extended as follows:

$$Jo = \frac{\lambda_{ref} \cdot \sigma_{abs}}{2\pi V} \tag{8}$$

Based on the above background, the calculation of relative photothermal conversion capability is not limited to spherical particles. Jo can be calculated by computing the optical absorption cross-section. Depending on the substrate type, LIPSS formed under femtosecond laser irradiation exhibit distinct periods and aspect ratios, which thereby result in varying optical absorption cross-sections under light irradiation. Accordingly, the relative photothermal conversion capability of different materials and different morphologies can be further evaluated.

3.2. Simulation of Photothermal Conversion Capability of ZrN

The optical responses of the isolated and periodic ZrN structures were investigated using the finite-difference time-domain method. A normally incident plane wave was used as the excitation source. Two orthogonal linear polarization states were considered, with the electric field oriented parallel and perpendicular to the long axis of the nanorod-like feature. The isolated capsule model was used to examine the intrinsic aspect-ratio-dependent response of an individual feature[34,35], whereas three-dimensional periodic-capsule and two-dimensional continuous-ridge models were introduced to evaluate the effects of inter-period coupling and structural

continuity. For the revised periodic comparisons, the wavelength range was restricted to 300–800 nm, over which the experimentally determined dielectric function of ZrN was available.

Because the solar simulator used in the photothermal experiments provides unpolarized illumination, the simulated absorption response used for comparison with the experiments was calculated as the equal-weight, incoherent average of the two orthogonal polarization components. For the three-dimensional models, the unpolarized effective absorption cross-section was calculated as：

$$C_{abs,unpolarized}(\lambda) = \frac{C_{abs,paralled}(\lambda) + C_{abs,perpendicular}(\lambda)}{2}$$

For the two-dimensional continuous-ridge models, the corresponding unpolarized absorption efficiency was calculated as:

$$Q_{abs,unpolarized}(\lambda) = \frac{Q_{abs,paralled}(\lambda) + Q_{abs,perpendicular}(\lambda)}{2}$$

This equal-weight averaging is appropriate for unpolarized illumination at normal incidence because unpolarized light contains equal, statistically incoherent power in any two orthogonal in-plane polarization components. The resulting absorption response is therefore invariant with respect to rotation of the in-plane coordinate axes, and no additional weighting based on the azimuthal orientation distribution is required for the linear optical response considered here.

The photothermal capability of ZrN nanorod structures with aspect ratios ranging from 1 to 50 was simulated. The range of 1–10 was defined as the low-aspect-ratio regime, while the range of 10–50 was defined as the high-aspect-ratio regime. Quantitative confocal analysis placed the Ti-based LIPSS at L/W = 8.47 ± 0.60, with individual-field values of 7.65–9.26. The Si-based LIPSS yielded L/W = 12.59 ± 2.01, with individual-field values of 10.58–14.48. Accordingly, the fabricated Ti structures correspond to the upper part of the simulated low-aspect-ratio regime, whereas the fabricated Si structures correspond to the lower part of the simulated high-aspect-ratio regime. The experimentally relevant simulated interval is therefore approximately L/W = 8–15. The wider simulated range was retained to establish the general aspect-ratio dependence beyond the presently fabricated structures. The absorption cross-sections obtained from the simulation are substituted into Equation 8. The variation of the dimensionless photothermal response parameter Jo with the incident wavelength is derived. The results are shown in 错误!未找到引用源。. A higher Jo value indicates a stronger relative photothermal conversion capability of the material.

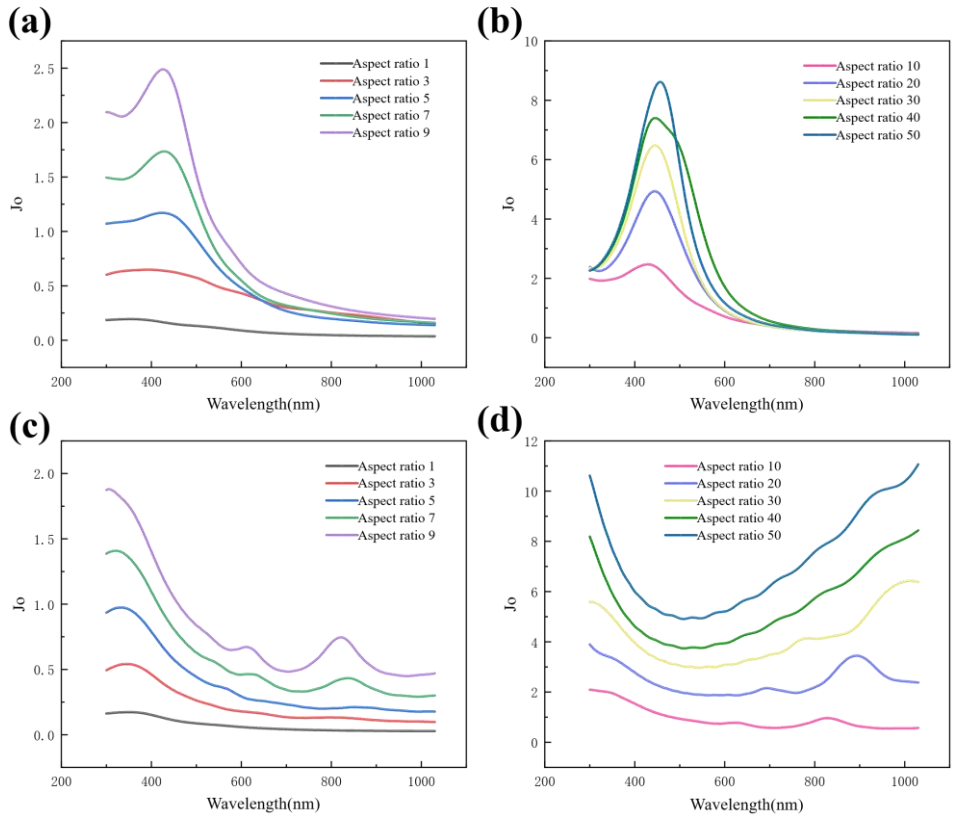


Fig. 2 Intrinsic aspect-ratio-dependent optical responses of the isolated ZrN capsule models. a,b, Dimensionless relative photothermal response parameter J_0 of isolated ZrN capsules in the low- (a) and high-aspect-ratio (b) regimes under an electric field parallel to the capsule long axis. c,d, Corresponding results in the low- (c) and high-aspect-ratio (d) regimes under an electric field perpendicular to the capsule long axis. These isolated-capsule calculations are used to identify intrinsic aspect-ratio-dependent trends rather than to quantitatively reproduce the periodic LIPSS.

Overall, when the polarization direction of the incident light is parallel to the long axis of the ZrN nanorods, continuous increases in the peak values are observed for all structures with increasing aspect ratio. In the low aspect ratio regime, the intensity of the photothermal response peak of the nanorods is significantly enhanced with increasing aspect ratio. The peak position is stably located in the visible light band. A slight red shift is observed in the peak position. Meanwhile, an obvious broadening trend is presented in the peak width. Almost no distinct peak is observed for spherical nanoparticles with an aspect ratio of 1, and extremely weak photothermal conversion capability is exhibited. When the aspect ratio reaches 9, the peak Jo value can exceed 2.5, and a significant longitudinal surface plasmon resonance effect is exhibited. All photothermal responses exhibit a single-peak characteristic, and the response in the long-wavelength region above 600 nm is monotonically attenuated with increasing wavelength. In the high aspect ratio regime, the peak width is further increased with further elevation of the aspect ratio. The response bandwidth is significantly broadened, which indicates that high aspect ratio structures can maintain efficient photothermal conversion over a wider wavelength range. The peak Jo value of nanorods with an aspect ratio of 50 can exceed 8.5, which is more than three times

that of structures with an aspect ratio of 10. Similar to the low aspect ratio system, the response peaks of the high aspect ratio system also possess a single-peak characteristic. The response in the long-wavelength region is rapidly attenuated, and no additional resonance peaks are observed.

These results indicate that when the polarization direction is parallel to the long axis of the nanorods, the longitudinal surface plasmon resonance of ZrN nanorods is effectively excited. A significant positive correlation is observed between the resonance intensity and the aspect ratio. The increase in aspect ratio enhances the local electric field enhancement effect of the nanorods. This further improves the light absorption efficiency and photothermal conversion capability and broadens the effective working wavelength band. Meanwhile, the influence of aspect ratio variation on the resonance peak position is limited. The response peaks are always concentrated in the visible light region.

When the polarization direction of the incident light is perpendicular to the long axis of the nanorods, the photothermal responses of nanorods with different aspect ratios exhibit significantly different characteristics compared with those under parallel polarization conditions. In the low aspect ratio regime, spherical particles with an aspect ratio of 1 still show no obvious resonance absorption. With the increase in aspect ratio, the intensity of the response peak near 400 nm gradually increases. When the aspect ratio is 9, the peak Jo value in the short-wavelength region is approximately 2.0. The intensity of the secondary peak in the long-wavelength region is approximately 0.8. A double-resonance characteristic is exhibited. In the high aspect ratio regime, with the increase in aspect ratio, the photothermal response of the nanorods presents a significant broadband characteristic. The response curve has no obvious single-peak structure. Instead, enhanced responses are observed in the short-wavelength region below 400 nm and the long-wavelength region above 800 nm. The Jo value of nanorods with an aspect ratio of 50 can exceed 10 near 300 nm. The Jo value remains around 11 near 1000 nm. A broadband photothermal response characteristic in both the ultraviolet and near-infrared regions is demonstrated. Meanwhile, the response intensity shows a monotonically increasing trend with increasing aspect ratio. The Jo values of the system with an aspect ratio of 10 are all below 2.5 across the entire wavelength band. The Jo value of the system with an aspect ratio of 50 can still be maintained above 11 in the near-infrared region.

The applicability of the isolated-capsule approximation was subsequently evaluated using periodic-boundary simulations. As illustrated in Supplementary Fig. S1a, the original isolated capsule was compared with a three-dimensional periodic array retaining the same geometry (L=1500 nm, W=150 nm, and L/W=10). Thus, the influence of periodic coupling could be evaluated without changing the capsule geometry or material properties. The polarization-resolved results are shown in Supplementary Fig. S1b and c. Relative to the isolated model, the spectrally averaged effective absorption cross-section of the near-contact periodic array (s/W=0.1) decreased by 36.33% under parallel polarization and by 13.17% under perpendicular polarization. In contrast, for s/W=1, the corresponding values increased by 19.24% and 25.40%, respectively. Supplementary Fig. S1d presents the equal-weight average

of the two orthogonal polarization responses, for which the near-contact array showed a 25.85% decrease relative to the isolated model, whereas the s/W=1 array showed a 22.03% increase. These results demonstrate that periodic coupling modifies both the magnitude and spectral profile of the optical response and cannot be represented by a constant correction to the isolated-particle result.

Because the experimental LIPSS are continuous surface features rather than assemblies of completely separated capsules, a two-dimensional continuous-ridge model was further constructed. The ridge width was fixed at W=150 nm, and the normalized transverse period was varied over Λ/W=1.10、1.25、1.50、2、3、5 and 8. The complete polarization-resolved and polarization-averaged spectra are presented in Supplementary Fig. S2a–c. Relative to the dilute periodic reference (Λ/W =8), the near-contact structure (Λ/W =1.1) exhibited decreases of 12.82% and 22.41% in the spectrally averaged absorption efficiency under parallel and perpendicular polarizations, respectively. The corresponding peak values decreased by 29.48% and 34.82%. After equal-weight averaging of the two polarization states, the near-contact structure exhibited an 18.22% decrease in the spectrally averaged absorption efficiency and a 29.59% decrease in the peak value. The quantitative spectral deviations and normalized responses are summarized in Supplementary Fig. S2 d–f. The response varied non-monotonically with (Λ/W =1.1), indicating that the effect of periodic coupling depends on separation as well as polarization.

The local electric-field distributions were further calculated at fixed wavelengths of 423 and 350 nm to clarify the spatial origin of the coupling-induced spectral differences. At 423 nm, reducing Λ/W from 8 to 1.1 decreased the mean inter-ridge field intensity by 56.9% under parallel polarization and by 22.8% under perpendicular polarization (Supplementary Fig. S3). Within the 30 nm shell outside the ZrN surface, the corresponding changes were +0.2% and −27.5%, respectively. At 350 nm, the mean inter-ridge field intensities decreased by 68.3% and 23.3%, whereas the corresponding surface-shell averages decreased by 11.9% and 19.4% (Supplementary Fig. S4). All comparisons within each supplementary figure were performed at a fixed wavelength using a common color scale. These results indicate that periodic coupling produces a wavelength-, spacing-, and polarization-dependent redistribution of the local field rather than a uniform enhancement or suppression.

These results indicate that when the polarization direction is perpendicular to the long axis of the nanorods, the transverse surface plasmon resonance of ZrN nanorods is excited. The increase in aspect ratio induces a transition in the resonance mode. In the low aspect ratio range, the transverse resonance intensity is relatively weak. The response characteristic is still dominated by a single peak in the visible light region. In the high aspect ratio range, the high aspect ratio structure of the nanorods can simultaneously excite high-order transverse resonance modes. A broadband response characteristic is formed. Efficient photothermal conversion from the ultraviolet to the near-infrared band is achieved. The above phenomena have also been observed and reported in many related studies [36–40].

The isolated-capsule calculations indicate that the intrinsic optical response of an individual nanorod-like feature is strongly dependent on its aspect ratio. However, the

periodic-boundary simulations further demonstrate that the response of the complete LIPSS is also governed by the normalized period, polarization state, and electromagnetic coupling between adjacent structures. The isolated model is therefore retained only as a qualitative reference for the intrinsic aspect-ratio-dependent trend, whereas the interpretation of the experimental LIPSS is based on the periodic and polarization-averaged simulations. The photothermal behavior of the Si- and Ti-based samples should consequently be discussed as the combined result of structural morphology, periodic optical coupling, and substrate-dependent heat transfer. Accordingly, the polarization-resolved results are used to elucidate the anisotropic coupling mechanism, whereas all comparisons with the photothermal experiments are based on the equal-weight averaged absorption response.

To distinguish the optical contribution of the patterned substrate from that of the ZrN-coated structure, additional FDTD simulations were performed for bare smooth, bare LIPSS, ZrN/smooth, and ZrN/LIPSS configurations (Supplementary Fig. S7). Introducing LIPSS increased the 300–800 nm AM1.5G-weighted absorptance of bare Si and Ti by only 0.0066 and 0.0051, respectively. For the ZrN-coated structures, the corresponding increases were 0.0188 for Si and 0.0054 for Ti. Material-resolved calculations further showed that the ZrN layer accounted for 90.0% and 90.3% of the absorbed optical power in the ZrN/LIPSS–Si and ZrN/LIPSS–Ti structures, respectively. These results indicate that LIPSS alone produces only a small absorption change in the bare substrates, whereas the enhanced response of the coated systems is primarily associated with the morphology-dependent optical response of the ZrN layer.

3.3. Photothermal Performance of ZrN Thin Films

Photothermal irradiation tests were recorded as continuous radiometric infrared-image sequences. The samples were oriented so that the irradiated top surface and one lateral edge were simultaneously visible. A fixed spot marker (SP1) was positioned near the center of the illuminated top surface to obtain the top-surface temperature or at the exposed lateral boundary corresponding to the film–substrate interface region to obtain the interface-region temperature. The selected position was maintained throughout each image sequence, and the SP1 value from each frame was exported to construct the temperature–time curve. The frame interval for the four-sample measurements was approximately 1.020–1.022 s. Because infrared thermography measures radiation from the visible surface, the interface-region value represents the apparent temperature at the exposed lateral boundary rather than a direct measurement inside the buried nanoscale interface. Each curve represents one continuous measurement for the corresponding sample and irradiation condition. The four substrates include the Si substrates with LIPSS, the Ti substrates with LIPSS, the smooth Si substrate and the smooth Ti substrate. The tests are carried out under 1 standard solar intensity(1 Sun, 100 mW/cm^2)for a continuous duration of 600 s. The temperature variations of the four samples at different time nodes are presented in Fig. 2.

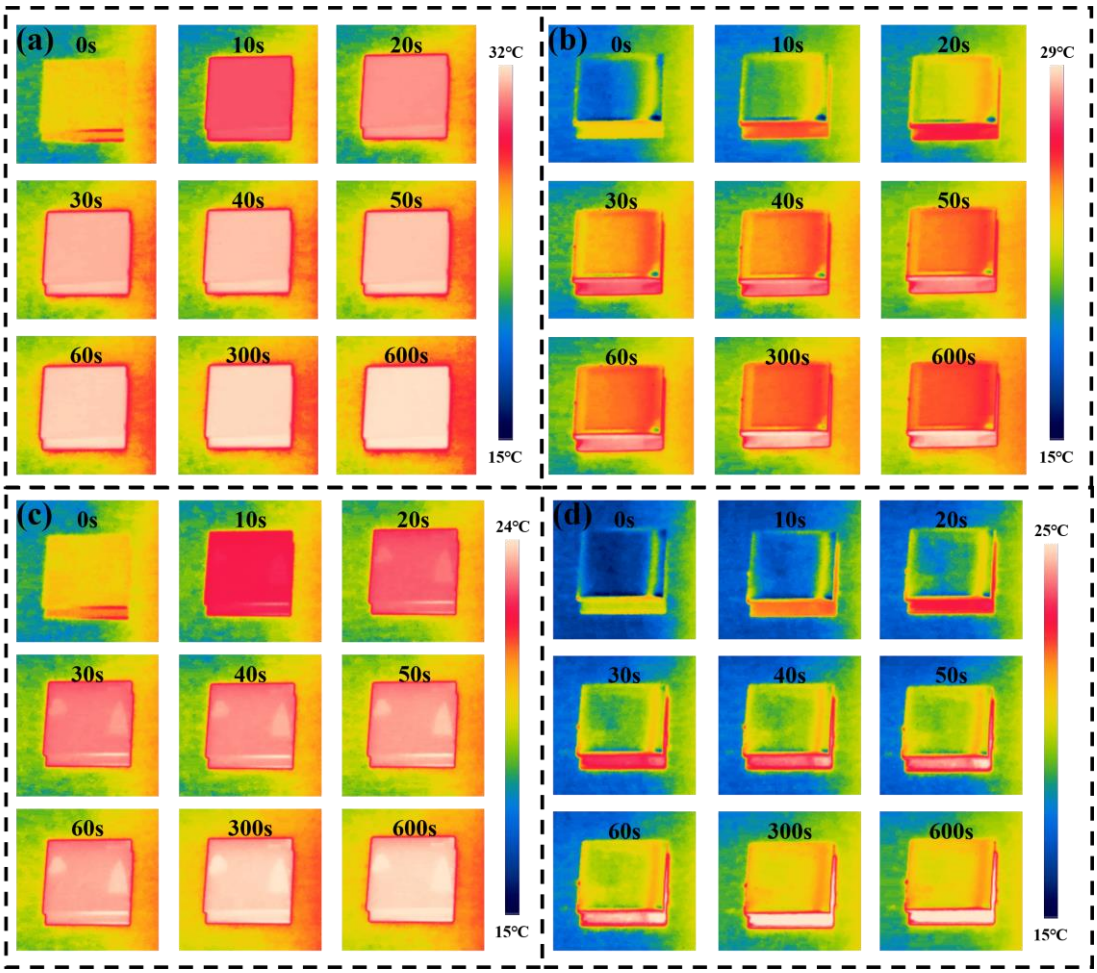


Fig. 2 Thermal images of ZrN thin films at different time nodes: (a) ZrN thin films on Si substrates with LIPSS; (b) ZrN thin films on Ti substrates with LIPSS; (c) ZrN thin films on smooth Si substrates; (d) ZrN thin films on smooth Ti substrates

Both the top and lateral end surfaces of four different ZrN thin film samples under simulated solar irradiation are displayed in the thermal images. Mechanistic differences in photothermal conversion and heat transfer modes are found between ZrN thin films on Si substrates and on Ti substrates according to Fig. 2. The temperature rise of ZrN thin films on Si substrates is first observed on the irradiated top surface regardless of the presence of LIPSS structures on the substrates. Heat is gradually transferred from the ZrN photothermal thin film layer to the Si substrate. The overall temperature of the samples is gradually homogenized over time. Such features are regarded as the typical photothermal conversion and substrate heat transfer characteristics of Si-based samples.

Remarkable differences are presented in the macroscopic heat transfer modes of ZrN thin films on Ti substrates. No obvious temperature increase is observed on the top surfaces of ZrN thin films with both Ti substrates with LIPSS and smooth Ti substrates when the light source irradiates the sample top surfaces. A distinct high-temperature layer is formed at the interface between the ZrN thin film and the Ti substrate. The temperature of the sample top surface is increased slowly over time. The temperature of the interface layer between the ZrN thin film and the Ti substrate

is raised rapidly. The temperature of the Ti substrate is increased quickly and falls between the temperatures of the top surface and the interface layer. The position of the maximum temperature is kept at the interface layer continuously until 600 s.

The top-surface and exposed interface-region temperatures of the four samples were extracted using fixed SP1 positions and plotted as functions of irradiation time. Each curve represents one continuous infrared measurement. The corresponding results are illustrated in Fig. 3.

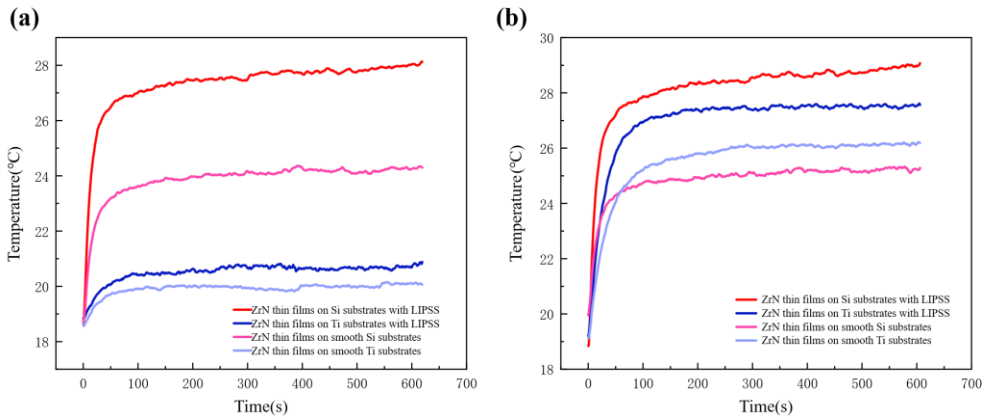


Fig. 3 Photothermal responses of ZrN thin film on four different substrates: (a) Surface temperature of the ZrN thin film; (b) Temperature at the interface between ZrN thin films and the substrates

Temperature increments to varying degrees are observed for ZrN thin film samples on four different substrates in Fig. 3(a). A certain photothermal conversion capability is inherently possessed by ZrN material. The photothermal conversion capability of ZrN material is further enhanced by the processing methods regulated by different substrates. All four samples complete the temperature rise within 100 s and then enter a relatively stable state with slight fluctuations. The two samples with Si substrates exhibit the fastest heating rate and finish the rapid temperature rise within 60 s. The two samples with Ti substrates reach a stable state at approximately 80 s.

Comparisons between Fig. 3(a) and Fig. 3(b) show that the temperature variations at the top surfaces and interfaces are basically consistent for the two Si-based samples. Obvious differences are presented for the two Ti-based samples. These differences are attributed to the intrinsic properties of the two materials. The thermal conductivity of Si is approximately 150 W/m·K, while that of Ti is about 15 W/m·K. A tenfold difference is exhibited between the two values. The heat transfer efficiency of Si is much higher than that of Ti. Heat is rapidly transferred in Si-based samples when the energy of the light source is converted into heat by ZrN thin films and transmitted to the substrates. The highest temperature is formed at the top surface and decreases gradually downward. Heat generated by the photothermal conversion of ZrN thin films cannot be effectively transferred to the substrates in Ti-based samples. A temperature rise caused by massive heat accumulation is observed at the interface between ZrN thin films and Ti substrates. Materials with high thermal conductivity

are thus more conducive to exerting the photothermal capability of ZrN thin films in photothermal conversion applications.

Figure 4(b) shows that the ZrN-coated samples prepared on LIPSS-patterned substrates reach higher heating rates and final temperatures than the corresponding ZrN-coated smooth samples. The additional optical-control simulations show that LIPSS increases the weighted absorptance of the bare substrates by only approximately 1%, whereas the increase reaches 5.53% for ZrN/LIPSS–Si relative to ZrN/smooth Si. Approximately 90% of the optical power absorbed by the coated LIPSS structures within 300–800 nm is dissipated in the ZrN layer. These results support the conclusion that femtosecond-laser-induced LIPSS regulation enhances the optical absorption and photothermal response of the ZrN-coated structures. The difference between the Si- and Ti-based temperature responses is further influenced by substrate-dependent heat transfer.

Among samples with Si and Ti substrates, the smooth Si-based sample shows a faster heating rate but a lower temperature in the final stable stage than the smooth Ti-based sample. This result is consistent with the heat transfer modes discussed above. Heat generated by ZrN thin films is rapidly transferred to the substrate in Si-based samples due to the high thermal conductivity of Si. A stable state is reached within a short time. Massive heat is accumulated at the interface layer in Ti-based samples owing to the extremely low thermal conductivity of Ti. A slow temperature rise caused by heat accumulation over time is observed in addition to the interface temperature rise induced by downward heat transfer from ZrN thin films in the early stage of heat transfer. A longer time is thus required for Ti-based samples to enter the stable state, and a higher final temperature is obtained.

The higher stable temperature of the ZrN/LIPSS–Si sample should be understood from the coupled but distinct effects of optical absorption and thermal transport. Quantitative confocal analysis gave effective lateral aspect ratios of 12.59±2.01 for LIPSS–Si and 8.47±0.60 for LIPSS–Ti (Table S1). Consistently, introducing LIPSS increased the 300–800 nm AM1.5G-weighted absorptance of the ZrN-coated Si structure by 0.0188 (5.53%), compared with 0.0054 (1.58%) for the corresponding Ti structure (Fig. S7c). Material-resolved calculations showed that 90.0% and 90.3% of the weighted absorbed optical power was dissipated within the ZrN layers of the LIPSS–Si and LIPSS–Ti structures, respectively (Fig. S7d). These results indicate that the larger aspect ratio of the Si-based LIPSS produces a stronger morphology-induced optical enhancement. After optical absorption, the higher thermal conductivity of Si promotes more rapid heat transfer from the ZrN layer into the substrate and a more spatially uniform temperature distribution, whereas the lower thermal conductivity of Ti favours localized heat accumulation near the interface region. Therefore, the stable temperature is governed by the combined effects of structure-induced absorption, LIPSS aspect ratio, substrate-dependent heat transport, and heat loss to the surroundings, rather than by aspect ratio or thermal conductivity alone. The conclusions obtained in the simulation of Section 3.2 are further verified by these results. In addition, a great improvement in photothermal conversion capability

induced by substrate regulation via femtosecond laser is found in the Si-based system. A small temperature difference in the stable stage is observed between the ZrN thin films on Ti substrates with LIPSS and the ZrN thin films on smooth Ti substrates. This result is also caused by the heat accumulation effect at the interface.

3.4. Light Dependence of ZrN Thin Films Tailored on Substrates by Femtosecond Laser

To further investigate the light intensity dependence of photothermal conversion capability for ZrN thin film samples prepared via femtosecond laser substrate regulation, photothermal conversion experiments were conducted. The experiments were performed under continuous irradiation for 600 s at light intensities of 0.5, 1.0, 1.5, 2.0, and 2.5 Sun, using ZrN thin films on Si and Ti substrates with LIPSS as test samples. Thermal imaging results at different time nodes are obtained and displayed in Fig. 4.

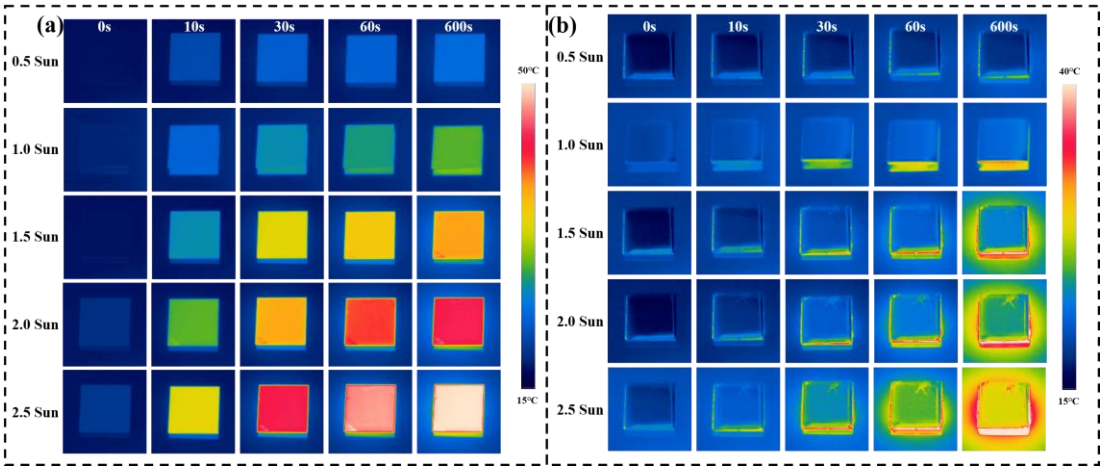


Fig. 4 Thermal images of ZrN thin films at different time nodes: (a) ZrN thin films on Si substrates with LIPSS; (b) ZrN thin films on Ti substrates with LIPSS

It can be found that the heat transfer modes of the two samples prepared by femtosecond laser-regulated substrates remain unchanged under the irradiation of simulated light sources with different intensities. A rapid temperature rise is achieved within 60 s. The maximum temperatures are presented on the light-irradiated top surfaces and at the interfaces between ZrN thin films and the substrates respectively. It is noteworthy that obvious distinctions are observed between the thermal imaging diagrams at 60 s and the images in the final stable state at 600 s as the light intensity increases. This phenomenon indicates that the maximum temperature of the samples is elevated sequentially with the increase of light intensity. The time required to reach the stable state is also prolonged gradually. Therefore, the top surface temperature of the ZrN thin films on Si substrates with LIPSS and the interface temperature of the ZrN thin films on Ti substrates with LIPSS are extracted separately for the plotting of temperature-time curves, as illustrated in Fig. 5.

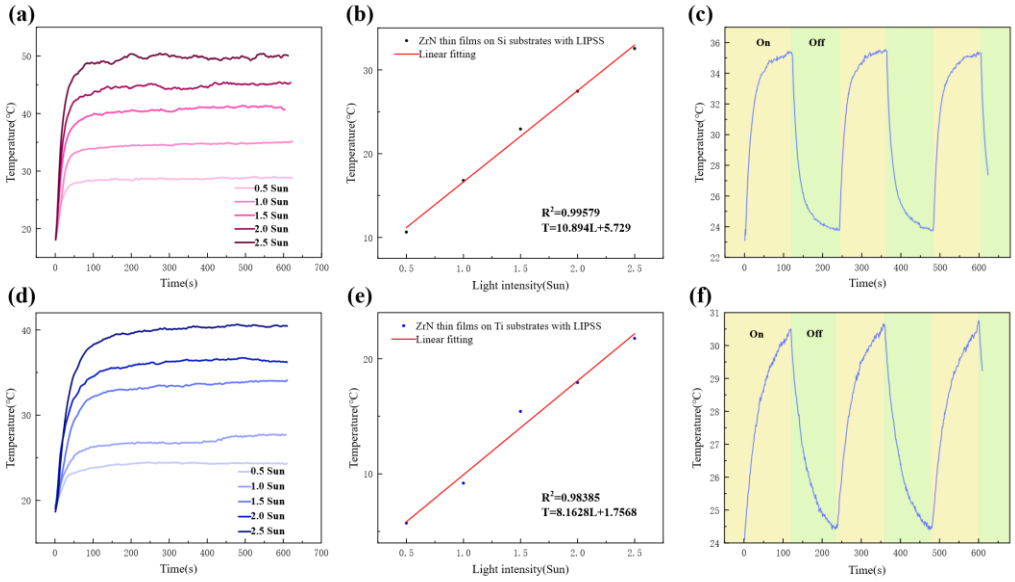


Fig. 5 For ZrN thin films on Si substrates with LIPSS: (a) Temperature variations under different light intensities; (b) Linearity between temperature rise range and light intensity; (c) Photocycling tests; for ZrN thin films on Ti substrates with LIPSS: (d) Temperature variations under different light intensities; (e) Linearity between temperature rise range and light intensity; (f) Photocycling tests

It can be observed from Fig. 5(a) and (d) that the steady-state temperatures of the two samples on LIPSS substrates are increased with the increase of light intensity. A temperature rise up to 31 °C is achieved for the ZrN thin films on Si substrates with LIPSS within 60 s under 2.5 Sun irradiation. The rate of temperature change in the initial heating stage is accelerated with the increase of light intensity. The time required to reach the steady state is prolonged accordingly. The time needed for the ZrN thin films on Ti substrates with LIPSS to reach the steady state is longer than that for the ZrN thin films on Si substrates with LIPSS under the same light intensity. The different heat transfer mechanisms of the two substrates are further verified by the above results.

Linearity analyses between the temperature rise range and light intensity are conducted to verify the dependence of the two samples on light intensity. The obtained results are shown in Fig. 5(b) and (e). The linearity coefficients between the temperature rise range and light intensity are calculated to be 0.996 for the ZrN thin films on Si substrates with LIPSS and 0.984 for the ZrN thin films on Ti substrates with LIPSS. Both values indicate a satisfactory linear relationship.

Multi-cycle photothermal cycling tests are carried out on the two samples on LIPSS substrates under 1 Sun irradiation to further investigate the time-dependent heating behavior. An alternating mode of 120 s light irradiation and 120 s light shut-off is adopted in the tests. Three consecutive light-on/light-off cycles were recorded within one continuous measurement. The close overlap of the heating and cooling responses demonstrates within-run cycling repeatability; these cycles are not treated as independent experimental replicates. The temperature responses to the switching on and off of the light source are presented in Fig. 5(c) and (f). Rapid responses to the switching on and off of the light source are exhibited by both samples. A rapid

temperature rise is achieved within tens of seconds when the light source is switched on. The temperature is reduced rapidly when the light source is switched off. The heating curves and cooling curves in multiple cycles are highly overlapped with each other. Extremely high consistency is maintained for the peak temperatures and cooling end-point temperatures. No obvious performance drift is detected. Excellent reversibility and stability in photothermal cycling are demonstrated by the samples.

Short-term photothermal repeatability was evaluated for the two ZrN/LIPSS samples under 1 Sun irradiation using three consecutive light-on/light-off cycles within one continuous measurement. Each cycle consisted of 120 s of irradiation followed by 120 s without irradiation. Both samples responded rapidly to switching of the light source, and the heating and cooling profiles remained similar over the three tested cycles without an obvious temperature drift. These results demonstrate short-term photothermal repeatability under the present test conditions, rather than long-term operational stability. Because no post-cycling structural or compositional characterization was performed, possible changes in morphology, phase, or chemical state after extended cycling cannot be assessed here. Longer-duration cycling accompanied by post-cycling characterization will be considered in future work.

The Si and Ti substrates required different laser-processing windows to form stable LIPSS because their responses to ultrashort-pulse irradiation are material dependent. Previous XPS and depth-resolved studies have shown that femtosecond-laser processing can alter the near-surface oxidation state of both Ti and Si. In the present work, all ZrN layers were deposited using the same compound target, working pressure, power density, target-to-substrate distance, substrate temperature, deposition time, and substrate rotation, thereby minimizing variability arising from the coating process; ZrN-film phase and microstructure are known to depend strongly on these deposition variables. The post-deposition confocal maps confirm preservation of the periodic surface relief, and the shallow measured relief ratios ($H/\Lambda = 0.130 \pm 0.016$ for Si and 0.071 ± 0.023 for Ti) make severe geometrical shadowing unlikely. Nevertheless, without sample-specific XPS/XRD and cross-sectional SEM, substrate-dependent interfacial chemistry, ZrN oxidation state or texture, and local thickness variation cannot be fully excluded. These factors may contribute to the detailed Si–Ti difference, whereas the observed enhancement of the LIPSS/ZrN systems relative to their corresponding smooth-substrate/ZrN controls remains experimentally established.

4. Conclusion and perspectives

In this study, the photothermal conversion characteristics and heat transfer mechanisms of ZrN thin films prepared by femtosecond laser substrate regulation combined with magnetron sputtering are systematically investigated. An innovative preparation scheme for photothermal ZrN thin films through femtosecond laser substrate regulation is proposed. LIPSS is induced on Si and Ti substrates by a 1030 nm femtosecond laser. ZrN thin films with a thickness of 200 nm are deposited afterward. Efficient processing is realized by this method. LIPSS are approximated as nanorods, and their structural features are characterized by the aspect ratio. The

photothermal responses of ZrN structures under different aspect ratios and polarization conditions are simulated by the FDTD method. The results show that the photothermal conversion capability of ZrN nanorods is in a significant positive correlation with the aspect ratio. Photothermal performance tests are carried out on four samples with different substrates by infrared thermal imaging technology. Totally different heat transfer mechanisms are found between Si and Ti substrates. Further light dependence experiments show that the temperature rise ranges of the two samples on LIPSS substrates present a good linear relationship with the incident light intensity. The linearity values reach 0.996 and 0.984 respectively. Excellent response speed and stability are exhibited in multi-cycle photothermal cycling tests. The heating and cooling curves of multiple cycles are highly overlapped. No obvious performance drift is observed. The synergistic regulation rules of structural aspect ratio and substrate thermal conductivity on the photothermal performance of ZrN thin films are revealed in this study. The heat transfer mechanisms under different substrate systems are clarified. This work therefore holds promising application potential in solar thermal conversion, photothermal therapy, and photothermal catalysis based on the above mechanistic findings.

Acknowledgment

This work was supported by the Strategic Priority Research Program of Chinese Academy of Sciences (Grant No. XDB0670100),National Key Research and Development Program of China (Grant No.2023YFB4605501), CAS Project for Young Scientists in Basic Research (Grant No. YSBR-056) , and National Natural Science Foundation of China (Grant No. 62175253).

References

[1] Yin M, Liang W, Miao Q, Yu H 2021 *Ceram. Int.* **47** 34072

[2] Ishii S, Yu M W, Chen K P, Nagao T 2023 *Adv. Mater. Interfaces* **10** 2201751

[3] Mayrhofer P H, Sonnleitner D, Bartosik M, Holec D 2014 *Surf. Coat. Technol.* **244** 52

[4] Liang D, Dai W 2023 *Scanning* **2023** 1

[5] Weihua F, Wang Yufei, Tang Bo, Zhang Sheng, Gu Xiaoyu, Li Hongfei, Sun Jun 2020 *Prog. Org. Coat.* **146** 105714

[6] Rakib A K M, Rahad R, Faruque Md O, Sagor R H 2023 *Opt. Express* **31** 25280

[7] Günaydın B N, Çetinkaya A O, Torabfam M, Tütüncüoğlu A, Kayalan C I, Bayazıt M K, Yüce M, Kurt H 2024 *Adv. Colloid Interface Sci.* **333** 103298

[8] Ijaz S, Rana A S, Ahmad Z, Rehman B, Zubair M, Mehmood M Q 2021 *Opt. Express* **29** 31537

[9] Traver E, Karaballi R A, Monfared Y E, Daurie H, Gagnon G A, Dasog M 2020 *ACS Appl. Nano Mater.* **3** 2787

[10] Pastukhov A I, Shipunova V O, Babkova J S, Zelepukin I V, Raab M, Schmitt R, Al-Kattan A, Pliss A, Kuzmin A, Popov A A, Klimentov S M, Prasad P N, Deyev S

M, Kabashin A V 2024 *ACS Appl. Nano Mater.* **7** 18737
[11] AlMehrzi M, Shaheen A, Ghazal A, Almarzooqi N, Raza A, Zhang T, AlMarzooqi F 2024 *J. Environ. Chem. Eng.* **12** 113763
[12] Singh N, Murugadoss V, Younis U, Shoukat T, Eric A, Manasa P, Caputo R, Neogi A, Wang Z 2024 *Chem. Eng. J.* **499** 156662
[13] Wang S, Gao Y, Liu Z, Yang C, An N, Meng H, Yan M, Qu G, Guo C 2020 *Eur. J. Pharm. Biopharm.* **149** 163
[14] Liu Y, Zhang X, Lu L, Ye J, Wang J, Li X, Bai X, Wang W 2022 *Chin. Chem. Lett.* **33** 1271
[15] Zhu D, Zuo P, Li F, Tian H, Liu T, Hu L, Huang H, Liu J, Qian X 2024 *Colloid Interface Sci. Commun*. **59** 100770
[16] Li Y, He G, Liu H, Wang M 2023 *Micromachines* **14** 913
[17] Song D, Wang J, Wu X, Gao L, Yang J, Liu X, Luo Q, Wang D, Wang Y 2024 *Micromachines* **15** 1101
[18] Tan J W, Wang G, Zhao G X, Hou Y C, Sun D R, Song Y F, Dong L Y, Zhao H, Wang Y 2022 *Front. Chem.* **10** 1082738
[19] Tan J, Wang G, Li Y, Yu Y, Chen Q 2023 *Laser Photonics Rev.* **17** 2200692
[20] Dong B, Xu Z, Shi C, Zhang K, Zhang Y, Hua R, Zhao W, Wang J 2023 *Opt. Laser Technol.* **163** 109338
[21] Feng J, Wang J, Liu H, Sun Y, Fu X, Ji S, Liao Y, Tian Y 2024 *Materials* **17** 3657
[22] Wang Q, Zhang R, Chen Q, Duan R 2024 *Micromachines* **15** 639
[23] Gao L, Zhang Q, Gu M 2025 *Int. J. Extreme Manuf*. **7** 022010
[24] Niu S, Wang W, Liu P, Zhang Y, Zhao X, Li J, Xiao M, Wang Y, Li J, Shao X 2024 *Photonics* **11** 857
[25] Ding Y, Wang C, Jia X, Liu L, Gao Z, Jiang X, Wang S, Yan D, Lin N, Li Z, Duan J 2026 *Int. J. Extrem. Manuf.* **8** 025004
[26] Ding Y, Jiang X, Wang C, Jia X, Liu L, Han W, Gao Z, Wang S, Lin N, Yan D, Duan J 2026 *Opto-Electron. Sci.* **5** 260004
[27] Jia X, Chen Y, Yi Z, Lin J, Luo J, Li K, Wang C, Duan J, Polyakov D S, Veiko V P 2026 *Light Adv. Manuf.* **7** 111
[28] Fraggelakis F, Lingos P, Tsibidis G D, Cusworth E, Kay N, Fumagalli L, Kravets V G, Grigorenko A N, Kabashin A V, Stratakis E 2025 *ACS Nano* **19** 23258
[29] Bonse J, Krüger J 2023 *Appl. Phys. A* **129** 14
[30] Wang B, Du M, Wang H, Wang M, Li D 2025 *Nanomaterials* **15** 1450
[31] Fedyaj V, Bronnikov K, Terentiev V, Simonov V, Simanchuk A, Babin S A, Yakubov A, Lazarenko P, Lapidas V, Pavlov D, Zhizhchenko A, Kuchmizhak A A, Dostovalov A 2025 *Surf. Interfaces* **78** 108162
[32] Baffou G, Quidant R 2013 *Laser Photonics Rev.* **7** 171
[33] Lalisse A, Tessier G, Plain J, Baffou G 2015 *J. Phys. Chem. C* **119** 25518
[34] Jia H, Fang C, Zhu X M, Ruan Q, Wang Y X J, Wang J 2015 *Langmuir* **31** 7418
[35] Cole J R, Mirin N A, Knight M W, Goodrich G P, Halas N J 2009 *J. Phys. Chem. C* **113** 12090
[36] García-Ramírez E V, Almaguer-Valenzuela S, Sánchez-Dena O,

Baldovino-Pantaleón O, Reyes-Esqueda J A 2016 *Opt. Express* **24** A154
[37] Fauzia V, Permana H E 2017 *J. Phys. Conf. Ser.* **817** 012009
[38] Meng L, Li Z, Deng Y 2021 *Gold Bull.* **54** 89
[39] Thambi V, Kar A, Ghosh P, Khatua S 2018 *J. Phys. Chem. C* **122** 24885
[40] Huang Y, Kim D H 2011 *Nanoscale* **3** 3228